Electronic Supplementary Material (ESI) for Nanoscale.

Blending functionalised ligands to form multivariate metal-organic nanosheets (MTV-MONs) with tuneable surface chemistry

David J. Ashworth[a] and Jonathan A. Foster*[a]

a. Dept. of Chemistry, The University of Sheffield, Dainton Building, Brook Hill, Sheffield, S3 7HF, UK.

Electronic Supplementary Information

Contents

1. MOF characterisation

1.1. 5,5*-MTV-MOF

Table S1. Elemental analysis of **5,5***-MTV-MOF

	Calculated / %			Observed / %		
	C	**H**	**N**	**C**	**H**	**N**
5,5*-MTV-MOF	50.57	6.15	2.95	50.80	6.19	2.64

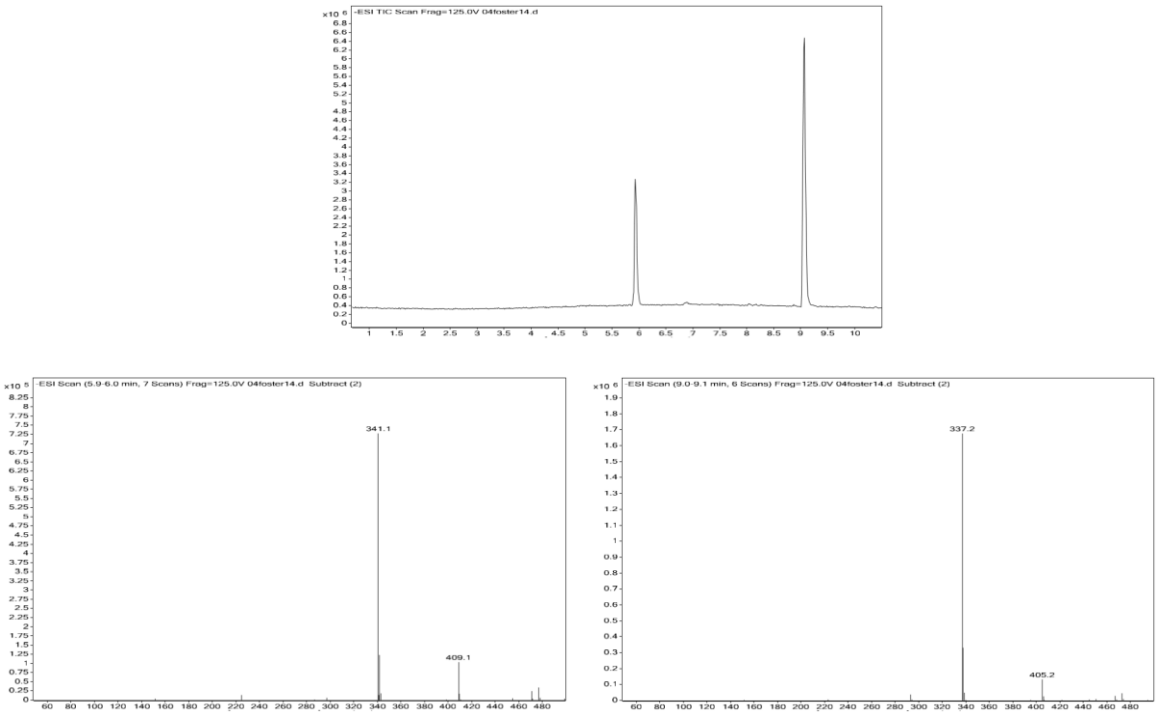

Figure S1. LC-MS data for digested **5,5***-MTV-MOF. Molecular ions for H**5***$^-$ and H**5**$^-$ appear at m/z= 341.1 and 337.2, respectively.

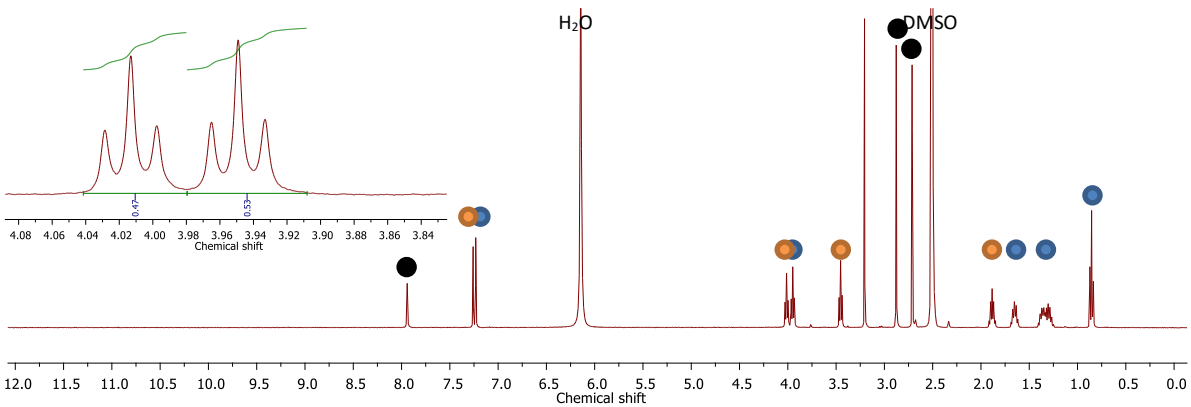

Figure S2. Room temperature ^{1}H NMR spectra of digested **5,5***-MTV-MOF, indicating a ligand ratio of **5** : **5*** of 0.53 : 0.47. Peaks corresponding to **5** (blue), **5*** (orange), DMF (black), DMSO and H_2O are indicated.

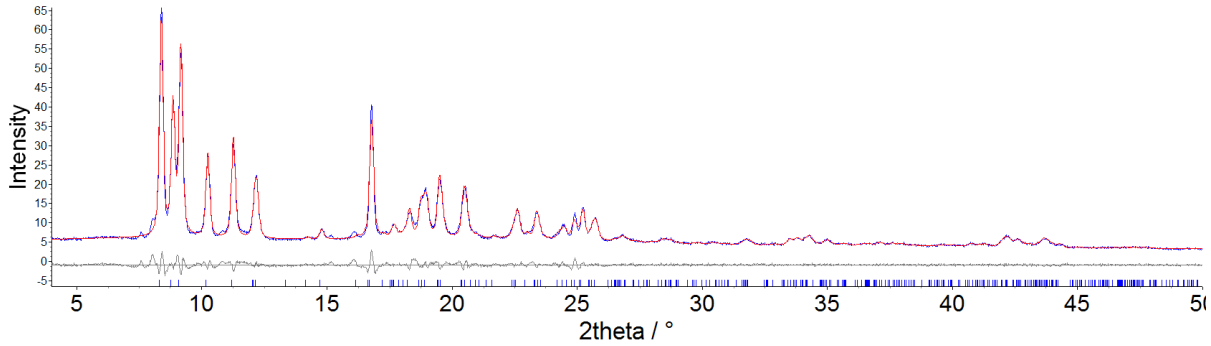

Figure S3. Pawley fits of 5,5*-MTV-MOF, illustrating the observed (blue) and calculated (red) diffraction patterns, with the difference plot [I_{obs}-I_{calc}] (grey) (2θ range 4.0 – 50.0 °, d_{min} = 1.82 Å). Blue tick lines denote calculated peak positions.

Table S2. PXRD refinement fitting data for **5,5***-MTV-MOF, compared with the previously published single-ligand MOFs structures.

MOF	Space group	a / Å	b / Å	c / Å	α / °	β / °	γ / °	Vol / Å^3	R_{wp}	$R_{wp'}$
Cu(**5**)(DMF)[1]	P-1	10.845	10.801	10.853	83.82	79.82	67.44	1154.4	0.0517	0.2455
5,5*-MTV-MOF	P-1	10.597(3)	10.803(2)	10.845(3)	85.65(3)	79.00(2)	68.90(1)	1137.0(5)	4.989	11.761
Cu(**5***)(DMF)[2]	P-1	10.525	10.762	10.807	85.29	77.11	68.26	1108.4	2.898	unreported

1.2. 3,5-MTV-MOFs

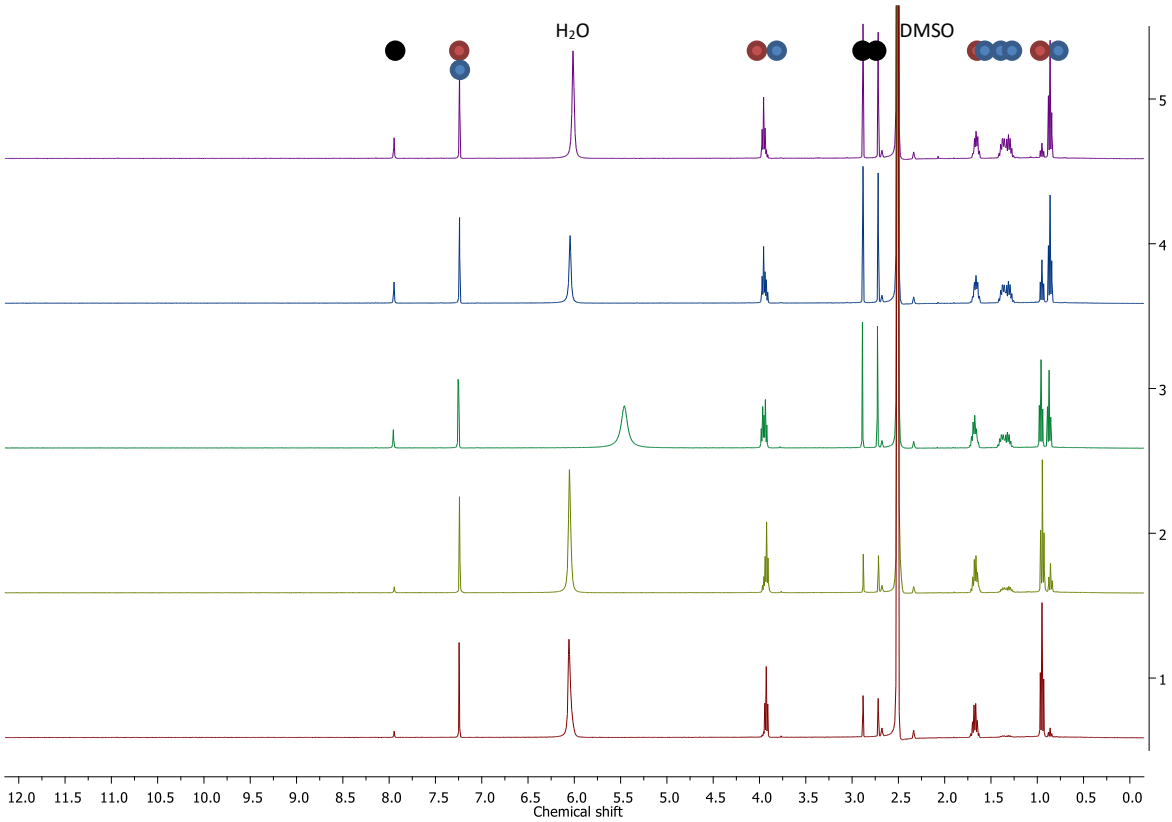

Figure S4. Room temperature ^{1}H NMR spectra of digested **3,5**-MTV-MOF blends. Peaks corresponding to **3** (red circle), **5** (blue circle), DMF (black), water and DMSO are indicated. Inset, the area used for ligand quantification.

Table S3. Ligand and DMF inclusion in Cu(**3**)$_x$(**5**)$_y$ blends.

Input / %		Observed / %		
3	**5**	**3**	**5**	**DMF***
10	90	14	86	83
25	75	29	71	76
50	50	52	49	63
75	25	79	21	24
90	10	90	10	28

* DMF % is reported relative to a total ligand:DMF ratio of 1:1, i.e. for a fully solvated structure.

1.3. Other binary blends

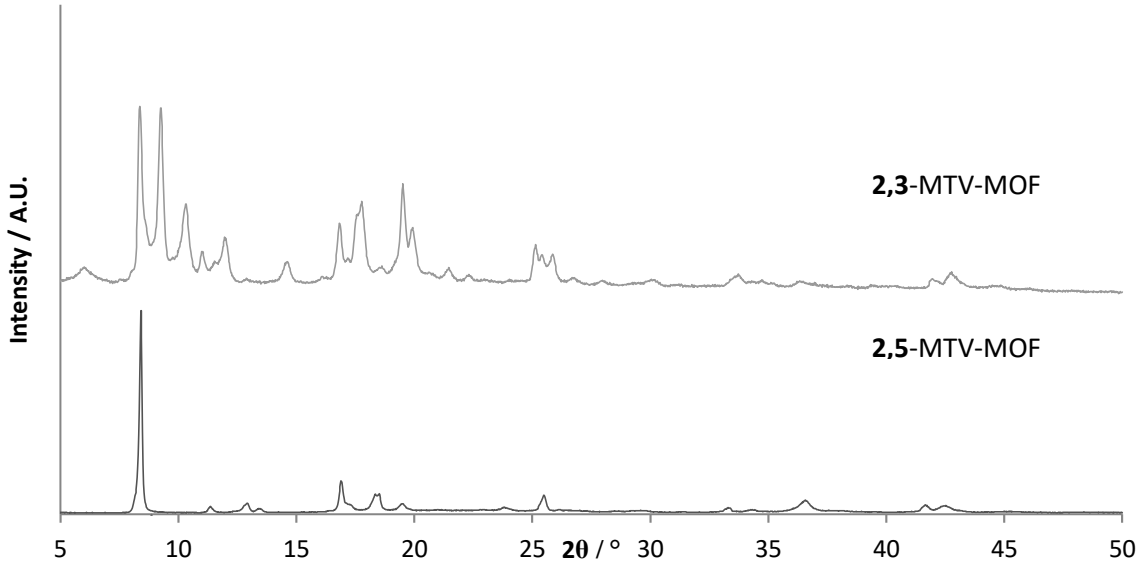

Figure S5. PXRD patterns of binary MTV-MOFs synthesised using combinations of ligands **2**, **3** and **5**.

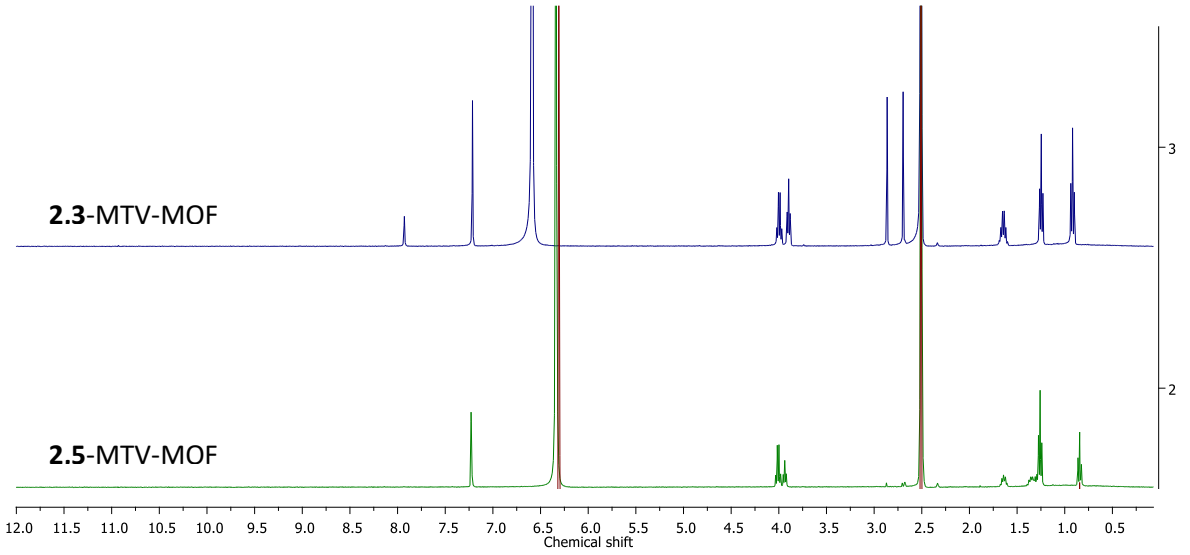

Figure S6. Room temperature ^{1}H NMR spectra of digested binary MTV-MOFs synthesised using combinations of ligands **2**, **3**, and **5**.

Table S4. Ligand and DMF inclusion MTV-MOF blends.

Input / %			Observed / %			
2	**3**	**5**	**2**	**3**	**5**	**DMF***
50	50		51	49		54
50		50	63		37	0

* DMF % is reported relative to a total ligand:DMF ratio of 1:1, i.e. for a fully solvated structure.

1.4. Tertiary and higher blends of MTV-MOFs

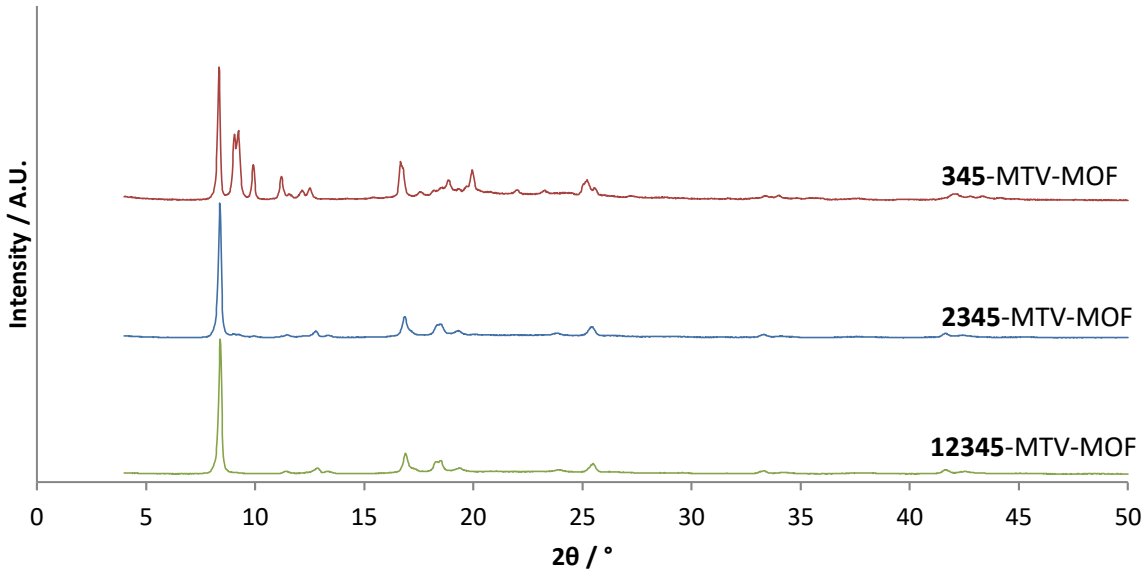

Figure S7. PXRD patterns of MTV MOFs synthesised using combinations of ligands **1**, **2**, **3**, **4** and **5**.

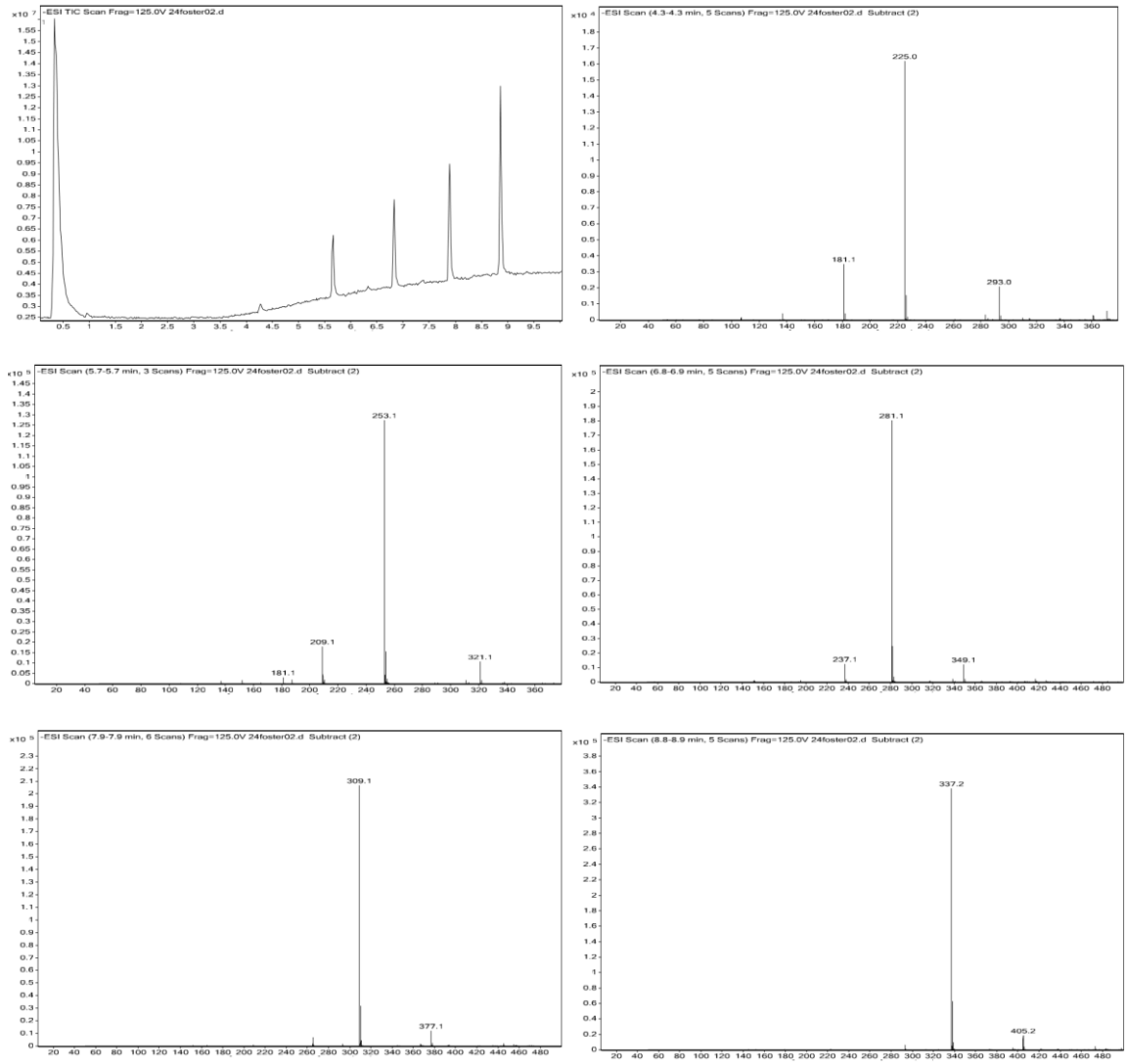

Figure S8. LC-MS spectra for **12345**-MTV-MOF

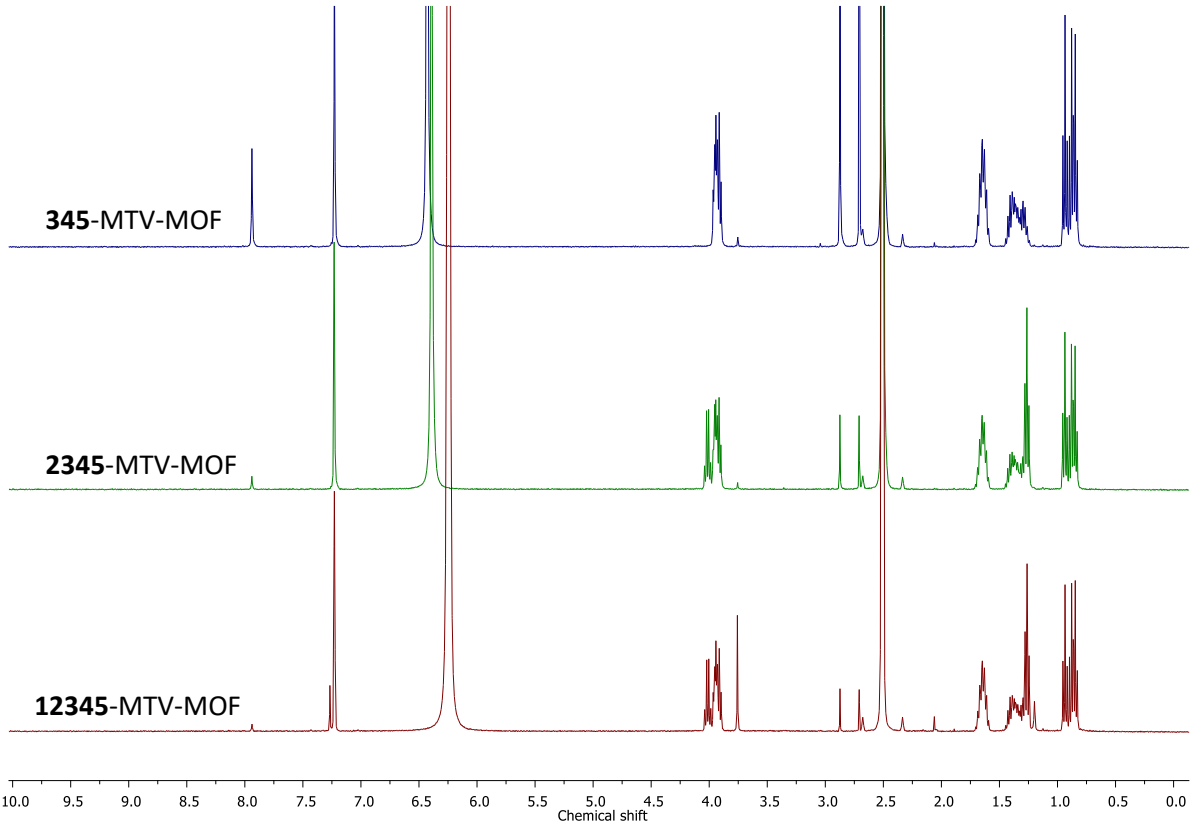

Figure S9. Room temperature 1H NMR spectra of digested MTV-MOFs synthesised using combinations of ligands **1**, **2**, **3**, **4** and **5**.

Table S5. Ligand and DMF inclusion within MTV MOFs

-MTV-MOF	Input					Observed					
	1	**2**	**3**	**4**	**5**	**1**	**2**	**3**	**4**	**5**	**DMF**
345			0.33	0.33	0.34			0.34	0.30	0.36	0.42
2345		0.25	0.25	0.25	0.25		0.22	0.22	0.27	0.29	0.09
12345	0.11	0.22	0.22	0.22	0.23	0.10	0.26	0.19	0.24	0.22	0.03

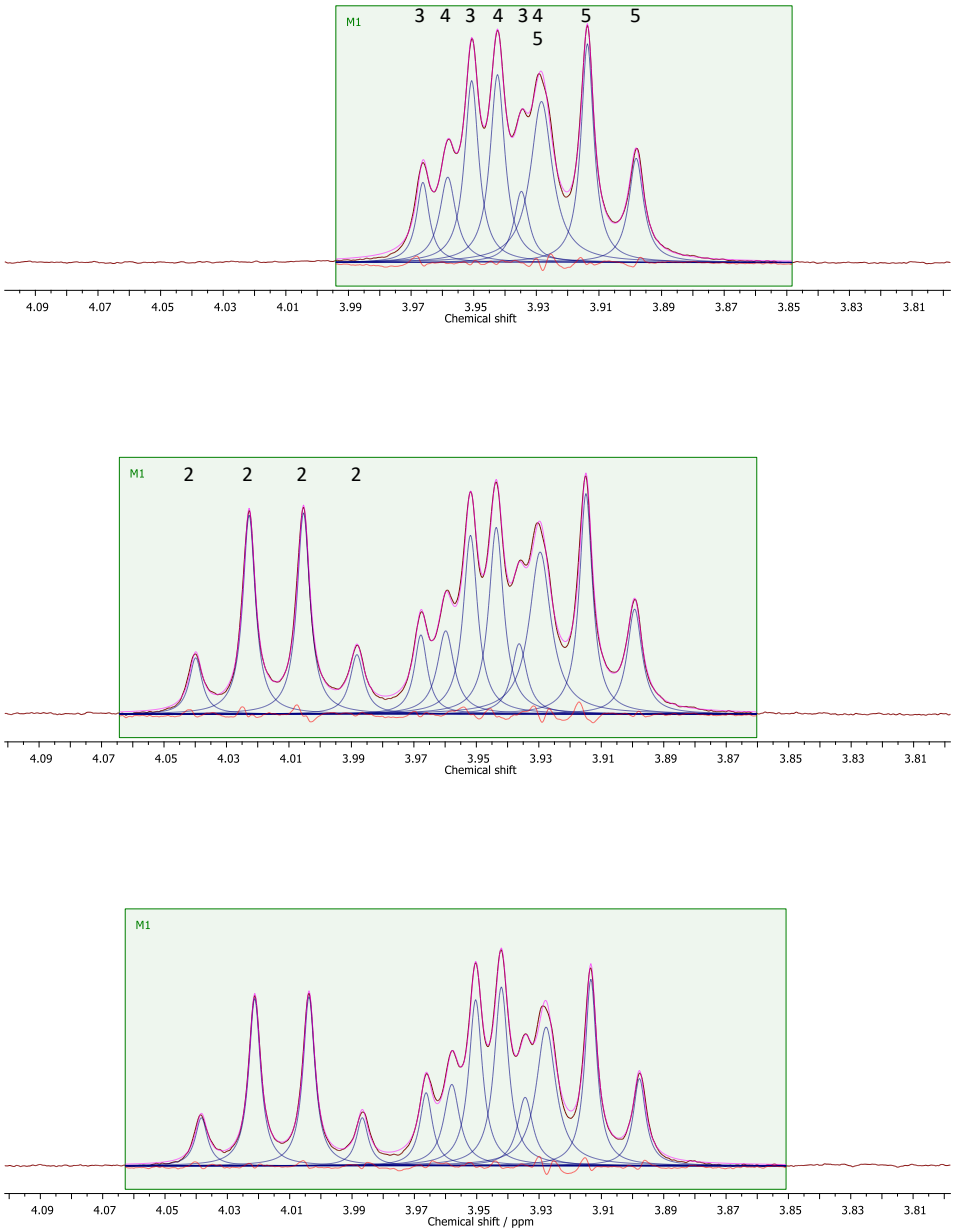

Figure S10. Peak fits used to quantify ligand inclusion in MTV-MOFs synthesised using combinations of ligands **1**, **2**, **3**, **4** and **5**, using spectra portrayed in Figure S9. Top-bottom: **345**-MTV-MOF, **2345**-MTV-MOF and **12345**-MTV-MOF.

2. MON characterisation

2.1.5,5*-MTV-MONs

2.1.1. ^{1}H NMR

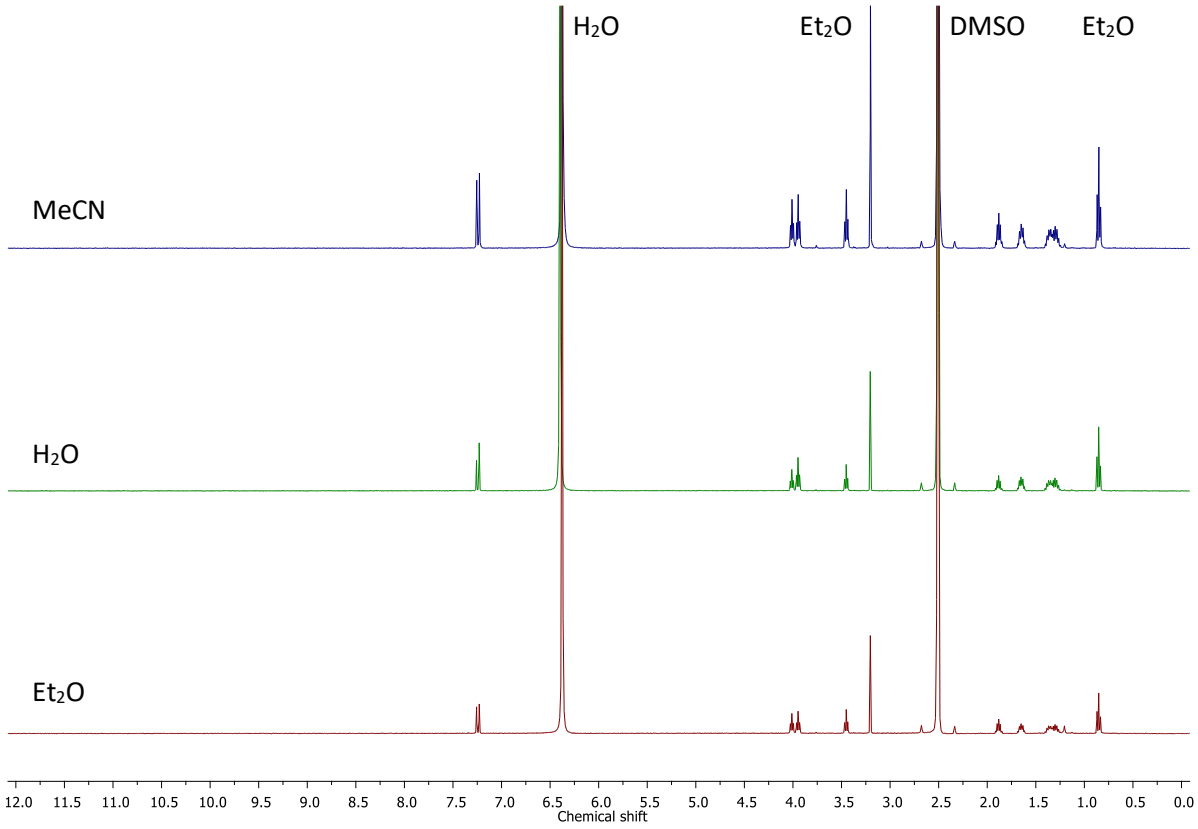

Figure S11. Room temperature 1H NMR spectra of **5,5***-MTV-MOF after exfoliation in MeCN, H_2O and Et_2O

2.1.2. PXRD

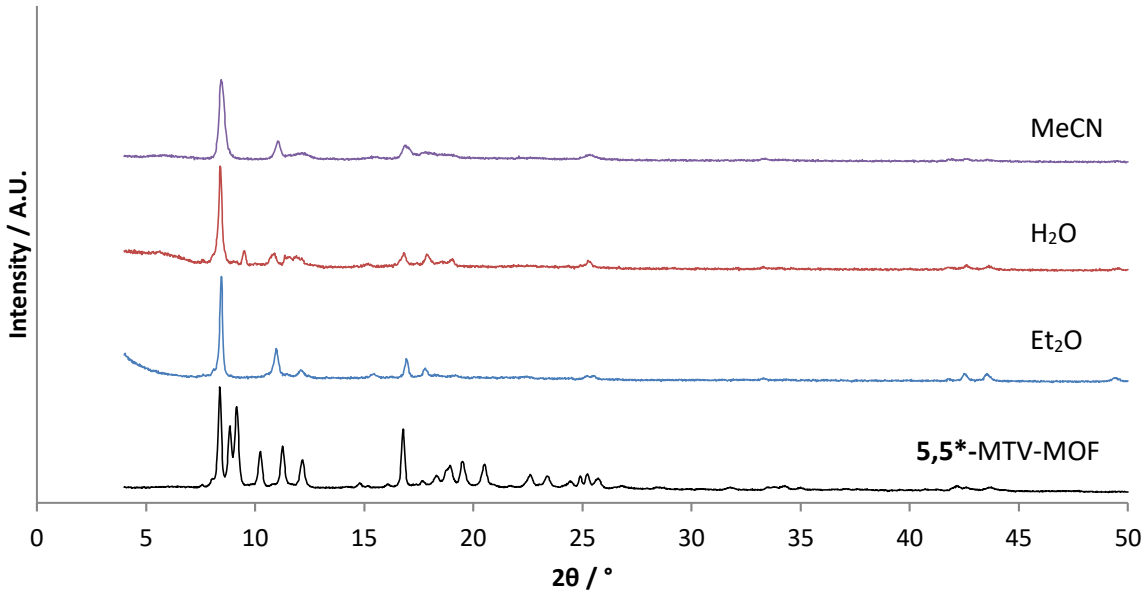

Figure S12. PXRD patterns of **5,5***-MTV-MOF after exfoliation in MeCN, H_2O and diethyl ether (Et_2O), compared to the input MOF.

2.1.3. XPS

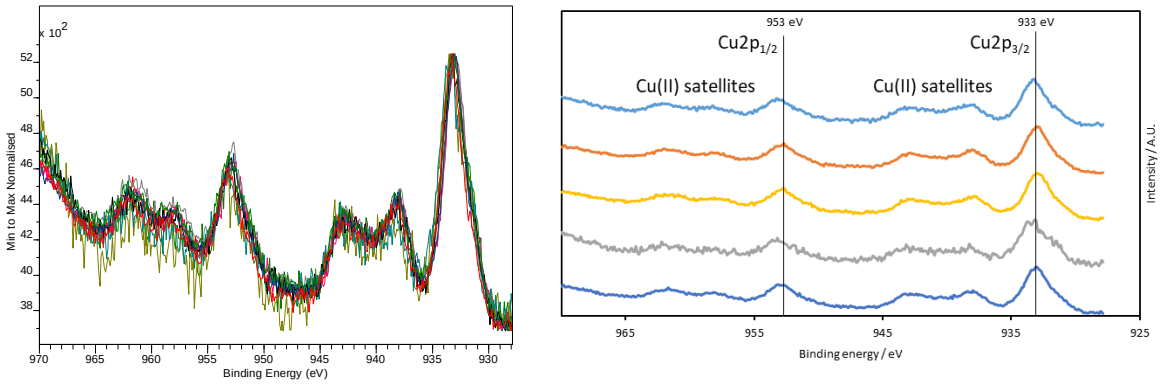

Figure S13. (Left) Overlay of unfitted high-resolution XPS spectra of the Cu2p region of the five samples analysed, with min-max normalisation. (Right) staggered plot showing normalised fitted data of 5,5*-MTV-MOF (top to bottom) as synthesised (blue, top), exfoliated in DMF (orange), MeCN (yellow), H_2O (grey) and Et_2O (dark blue).

2.1.4. FTIR spectroscopy

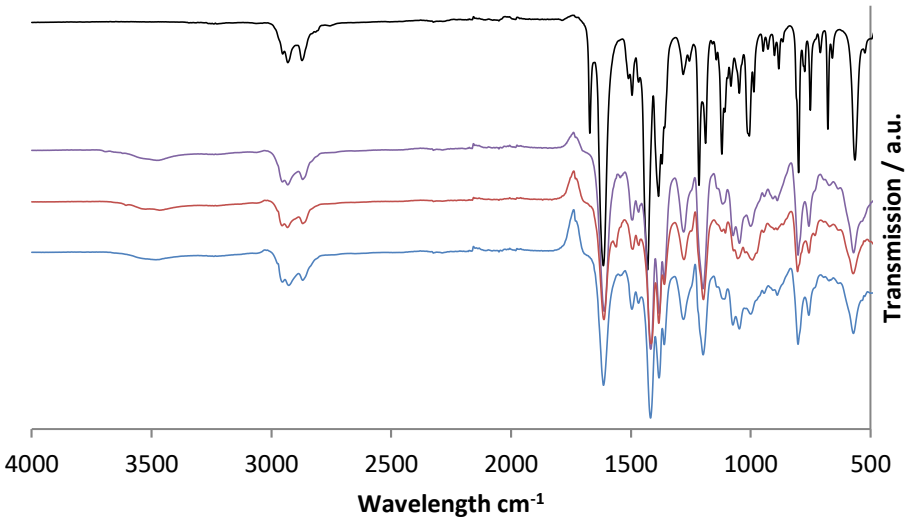

Figure S14. FTIR spectra of **5,5***-MTV-MOF (black) after exfoliation in MeCN (purple), H_2O (red) and Et_2O (blue). Note the absence of the C=O stretch at 1671 cm^{-1} in the exfoliated materials, indicating DMF loss.

2.1.5. UV-Vis

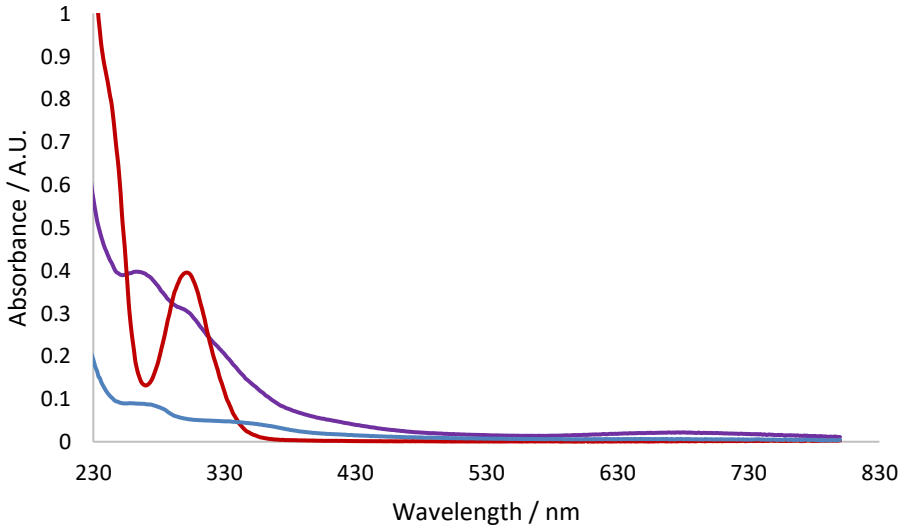

Figure S15. UV-Vis spectra of **5,5***-MTV-MOF after exfoliation in MeCN (purple), H_2O (red) and Et_2O (blue). Dilutions used were 1 in 6, 6 and 5, respectively.

2.1.6. AFM

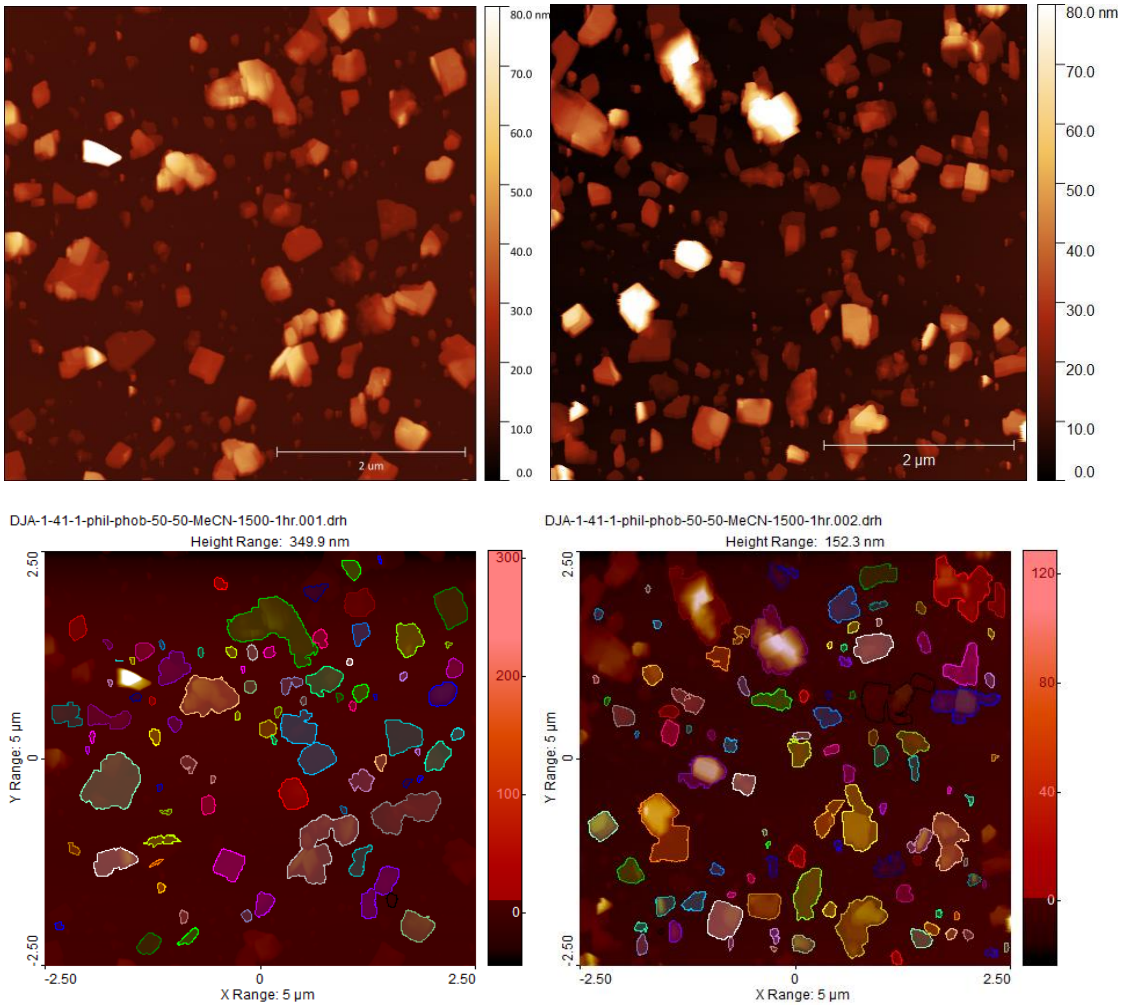

Figure S16. Cu(**5**)(**5***)(DMF) exfoliated in MeCN, after centrifugation at 1500 rpm for 1 hr, and automated particle identification.

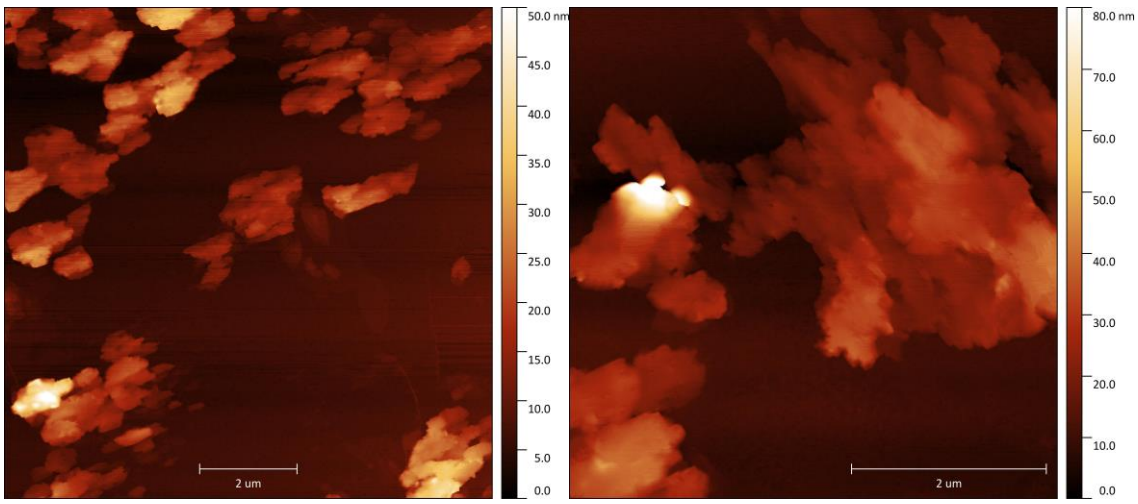

Figure S17. Cu(**5**)(**5***)(DMF) exfoliated in H_2O, after centrifugation at 1500 rpm for 1 hr.

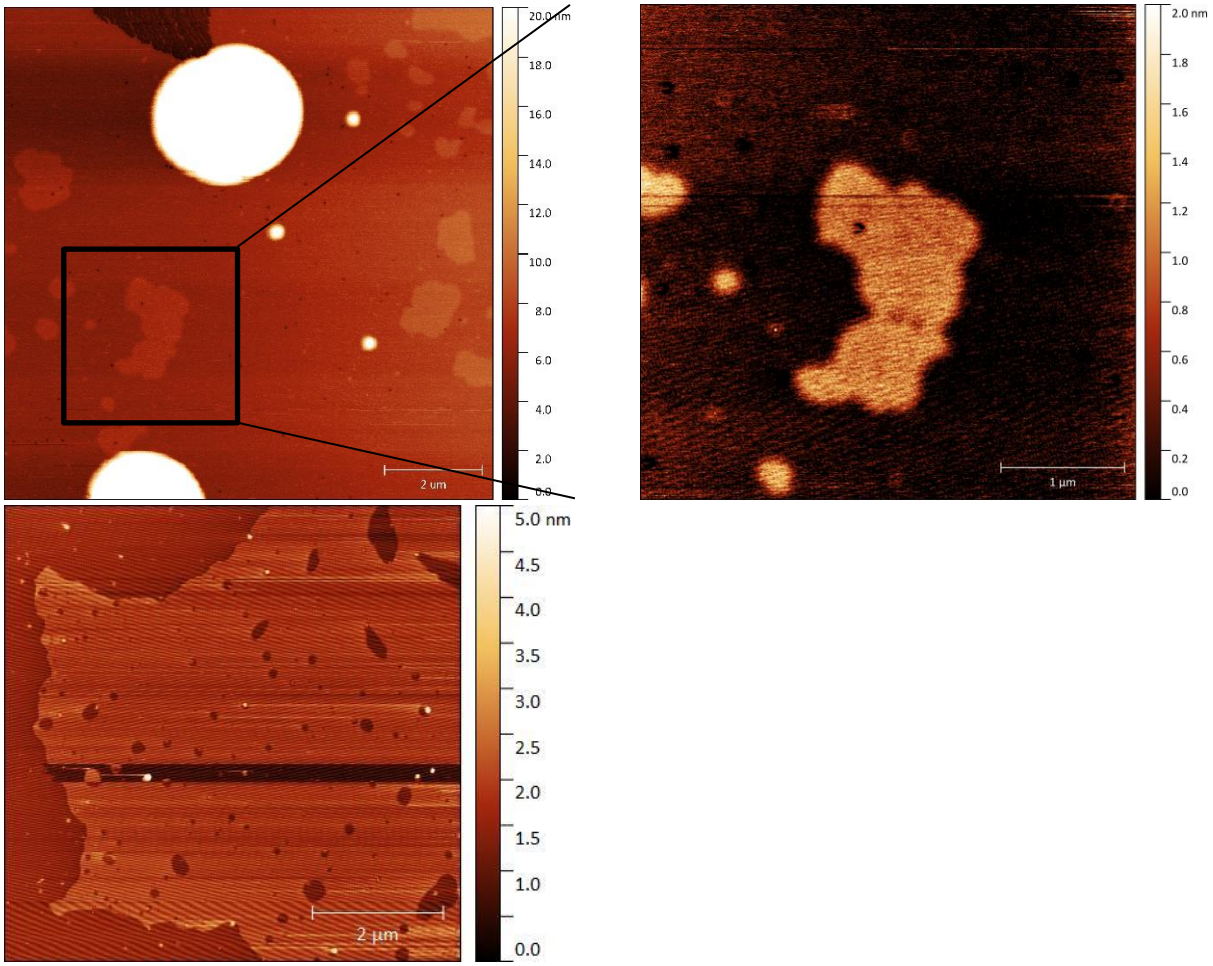

Figure S18. Cu(**5**)(**5***)(DMF) exfoliated in diethyl ether, after centrifugation at 1500 rpm for 1 hr.

2.1.7. Imidazole binding

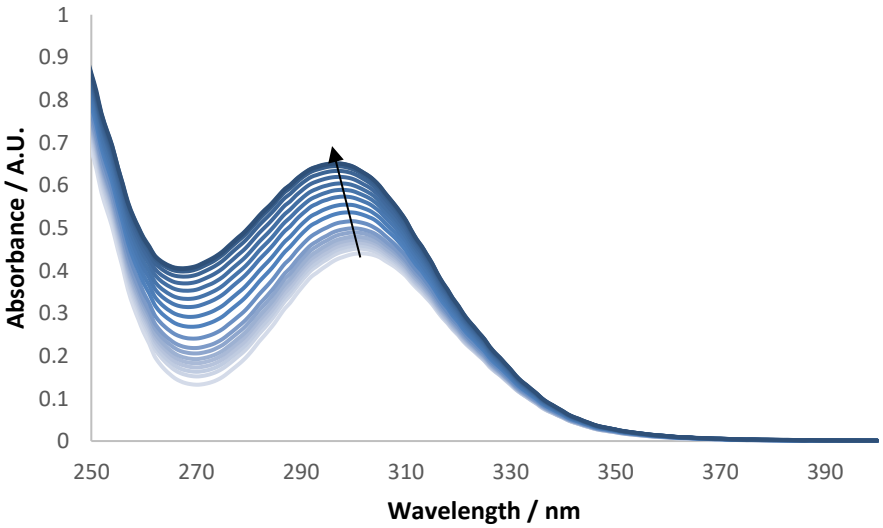

Figure S19. UV-Vis spectra showing the change in absorbance upon addition of aliquots of imidazole in MON suspension to a MON suspension.

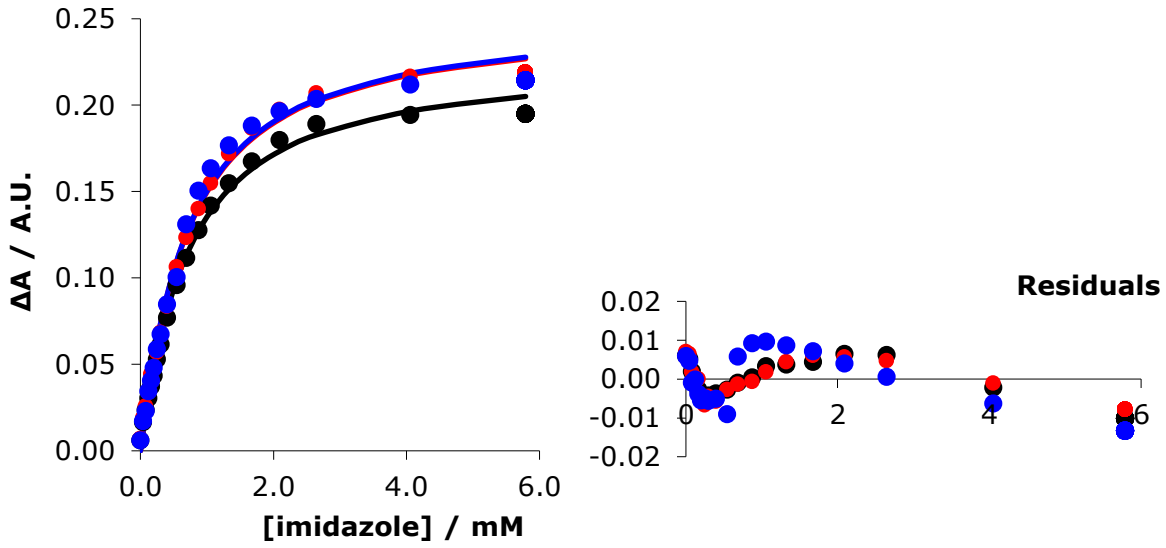

Figure S20. Change in absorbance at λ=302 nm for three repeat UV-Vis titrations of imidazole in MON suspension to MON suspension, fit to binding curves (left) , and residuals (right).

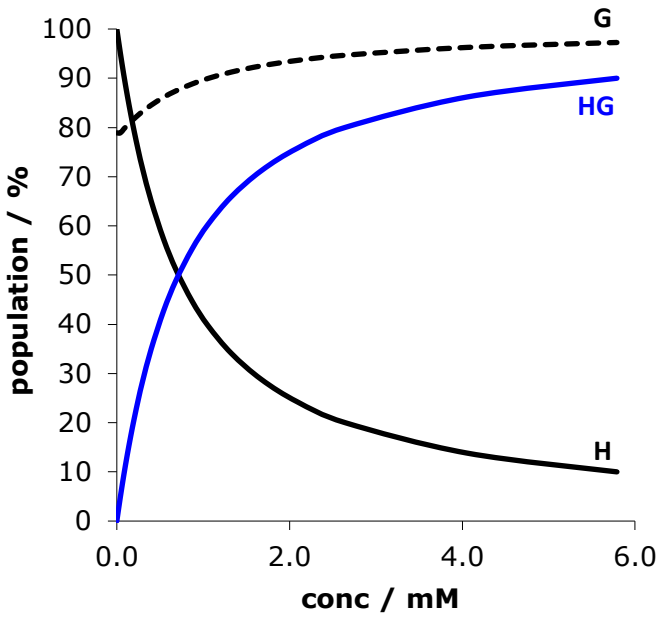

Figure S21. Speciation plot showing formation of **HG** complex upon addition of imidazole (**G**) to a suspension of Cu(**5**)$_{0.5}$(**5***)$_{0.5}$(H_2O) nanosheets (**H**).

2.2.Single-ligand parent MONs

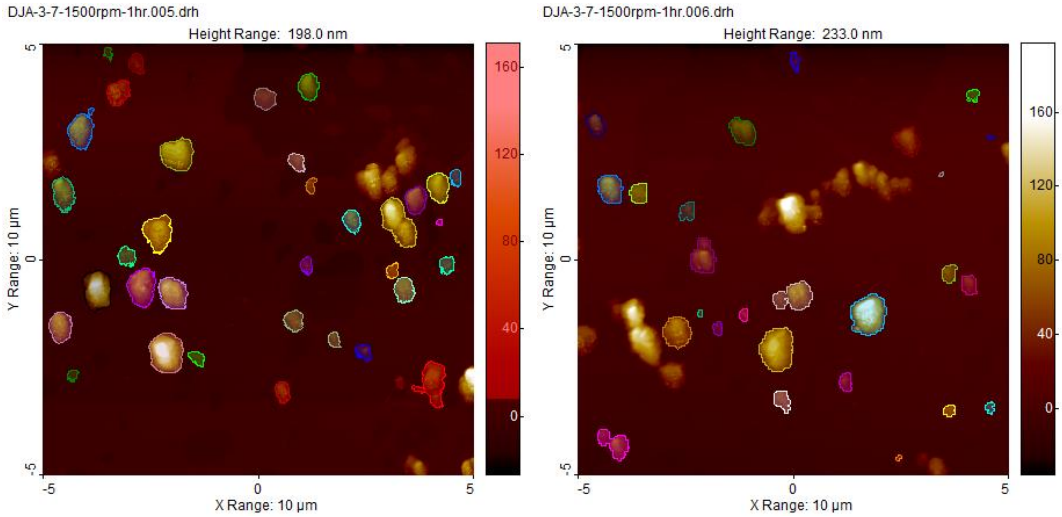

Figure S22. AFM topographical images of Cu(**5***)(DMF) exfoliated in MeCN and centrifuged at 1500 rpm for 1 hr,[3] and automated particle identification.

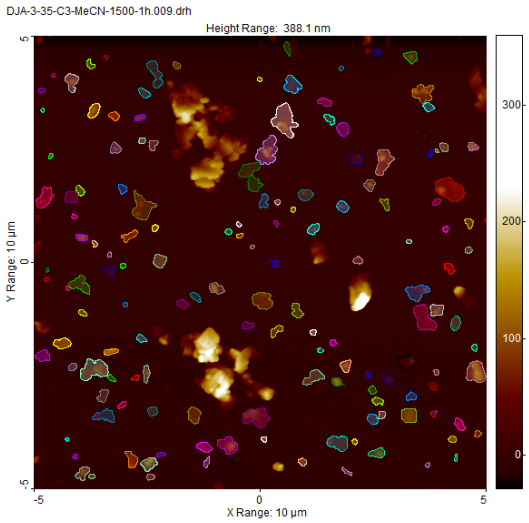

Figure S23. AFM topographical images of Cu(**3**)(DMF) exfoliated in MeCN and centrifuged at 1500 rpm for 1 hr,[1] and automated particle identification.

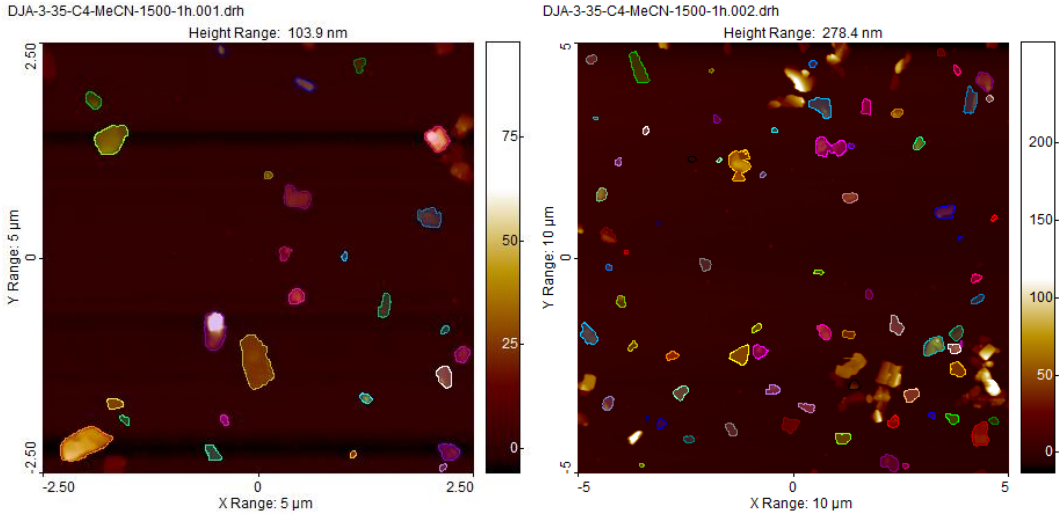

Figure S24. AFM topographical images of Cu(**4**)(DMF) exfoliated in MeCN and centrifuged at 1500 rpm for 1 hr,[1] and automated particle identification.

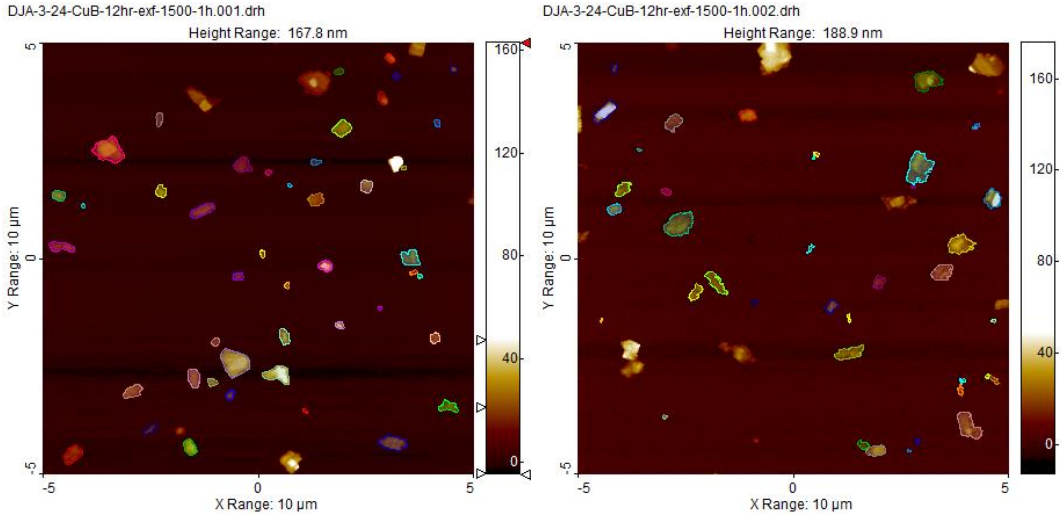

Figure S25. AFM topographical images of Cu(**5**)(DMF) exfoliated in MeCN and centrifuged at 1500 rpm for 1 hr,[1] and automated particle identification.

2.3.Cu(3)$_x$(5)$_y$ blends

2.3.1. PXRD

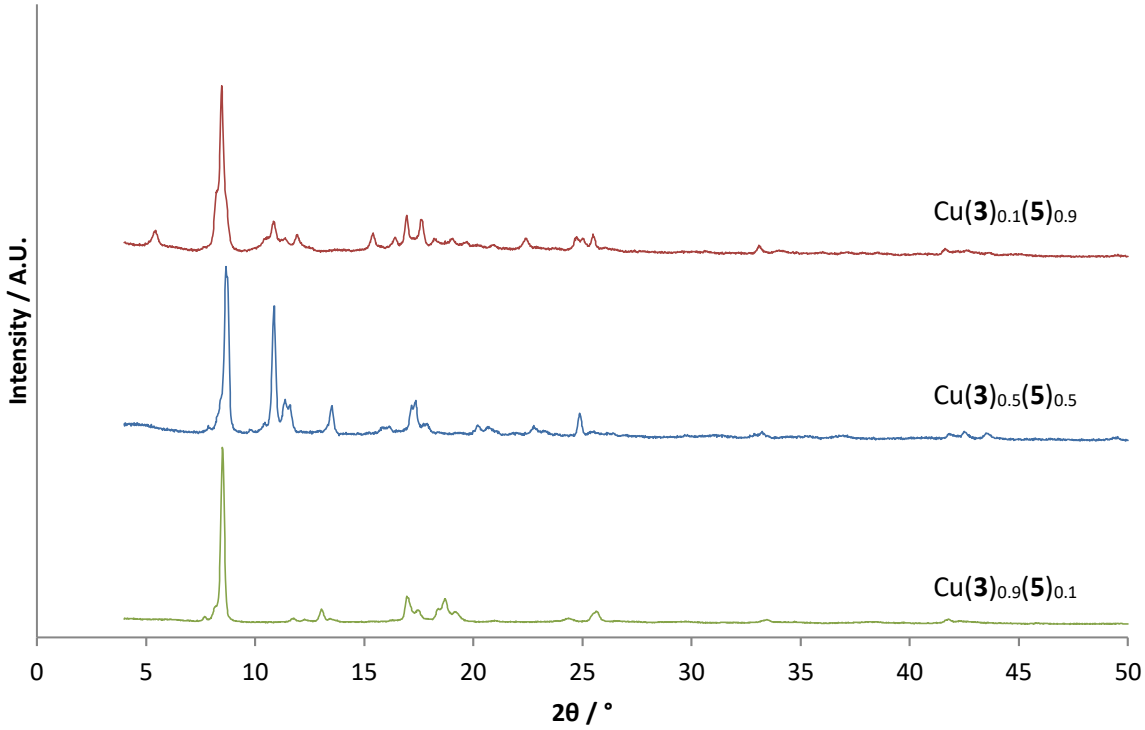

Figure S26. PXRD patterns of Cu(**3**)$_x$(**5**)$_y$ blends after exfoliation in MeCN.

2.3.2. AFM

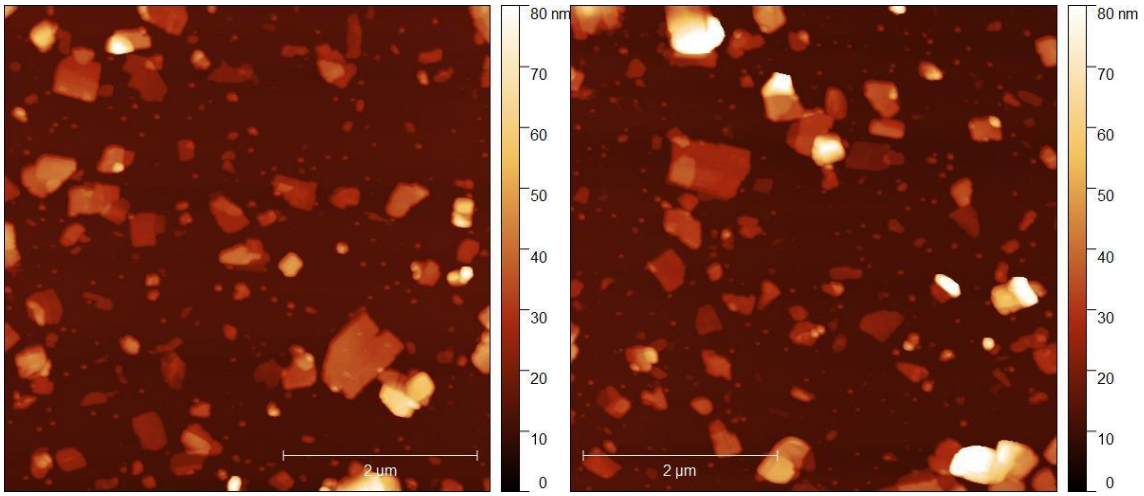

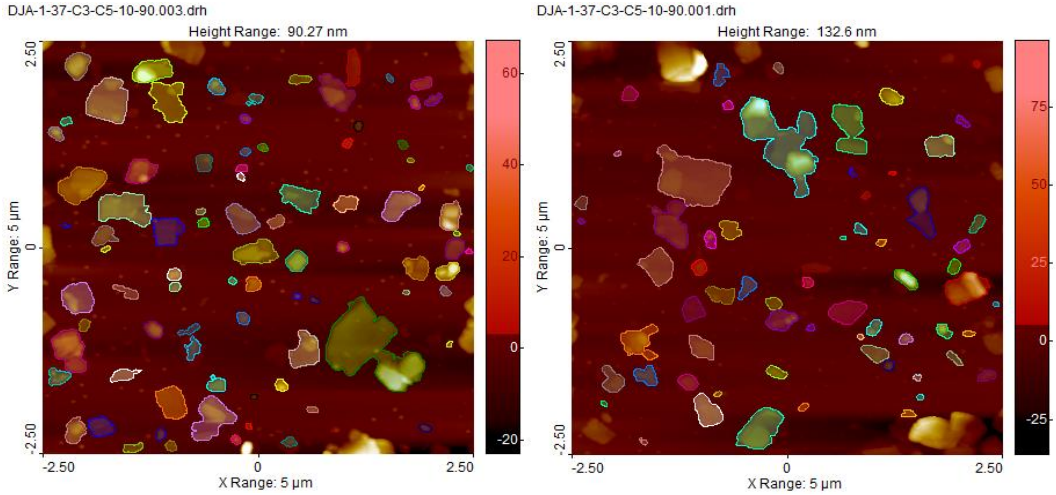

Figure S27. AFM topographical images of Cu(**3**)$_{0.1}$(**5**)$_{0.9}$ exfoliated in MeCN and centrifuged at 1500 rpm for 1 hr, and automated particle identification.

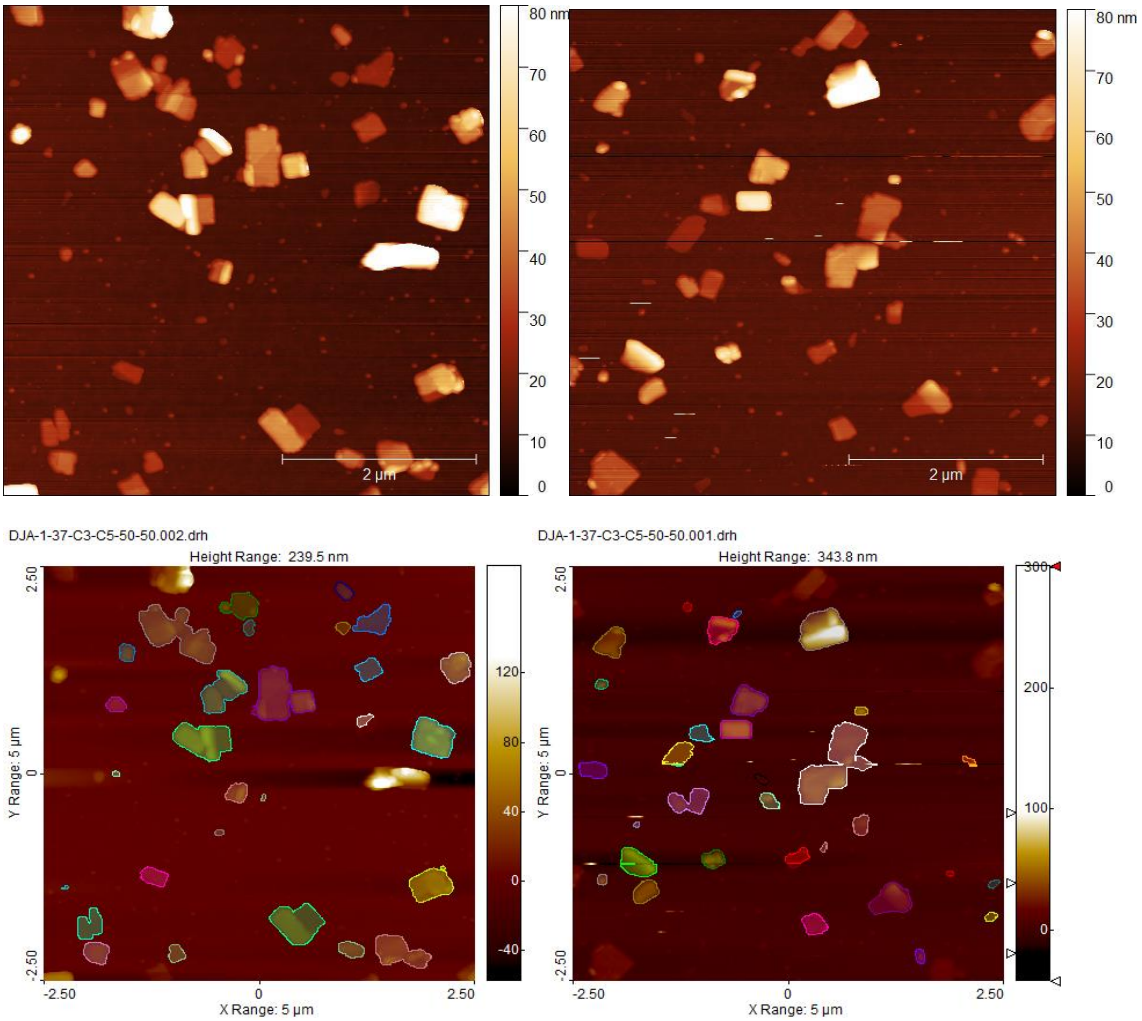

Figure S28. AFM topographical images of Cu(**3**)$_{0.5}$(**5**)$_{0.5}$ exfoliated in MeCN and centrifuged at 1500 rpm for 1 hr, and automated particle identification.

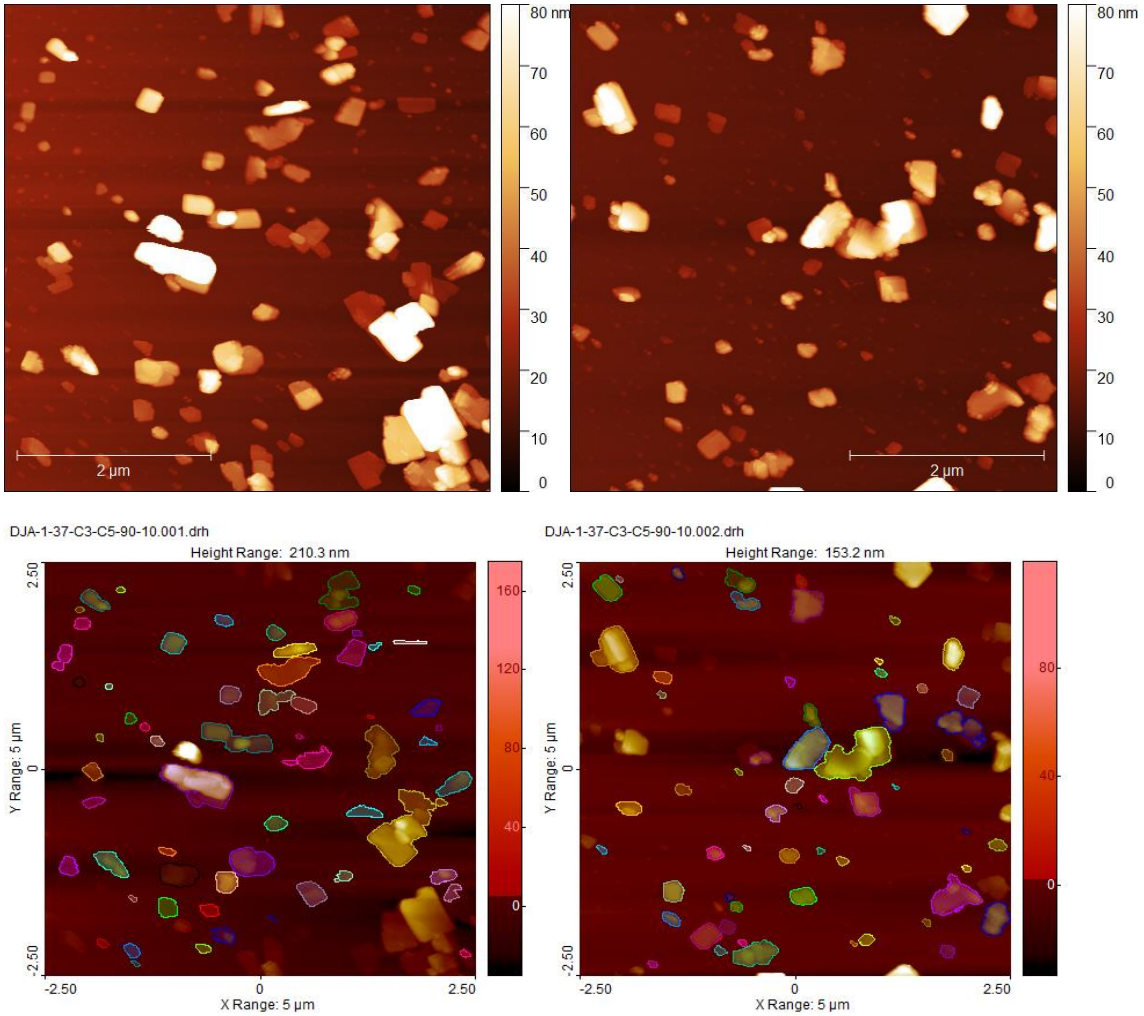

Figure S29. AFM topographical images of Cu(**3**)$_{0.9}$(**5**)$_{0.1}$-MTV-MOF exfoliated in MeCN and centrifuged at 1500 rpm for 1 hr, and automated particle identification.

2.4.Other binary blends

2.4.1. PXRD

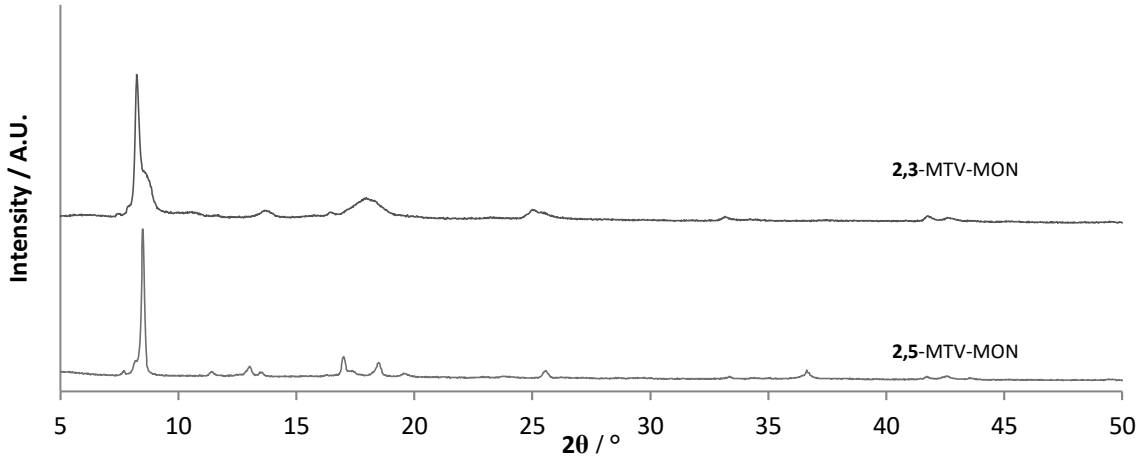

Figure S30. PXRD patterns of binary MTV-MOFs after exfoliation in MeCN.

2.4.3. AFM

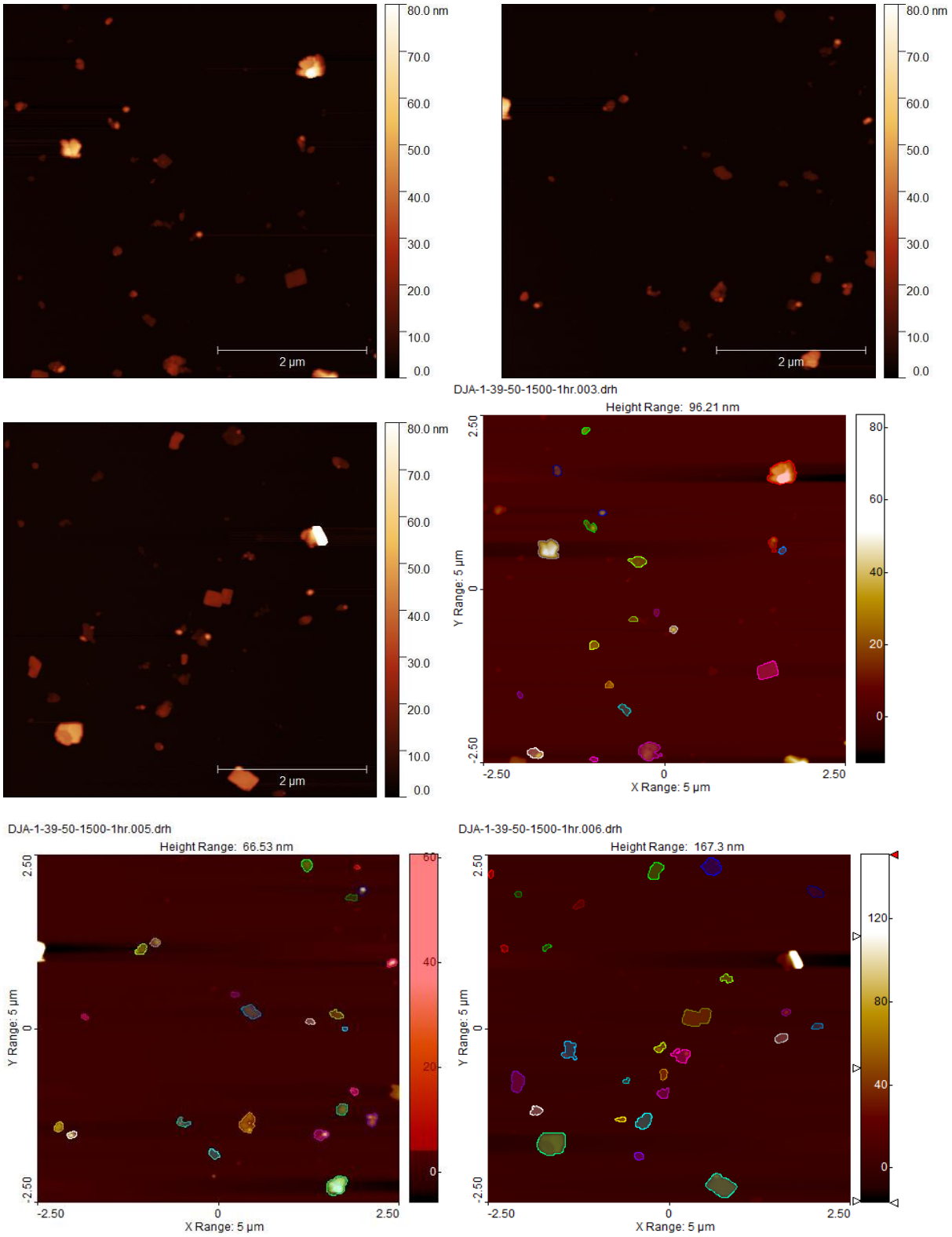

Figure S31. AFM topographical images of **2,3**-MTV-MOF exfoliated in MeCN and centrifuged at 1500 rpm for 1 hr, and automated particle identification.

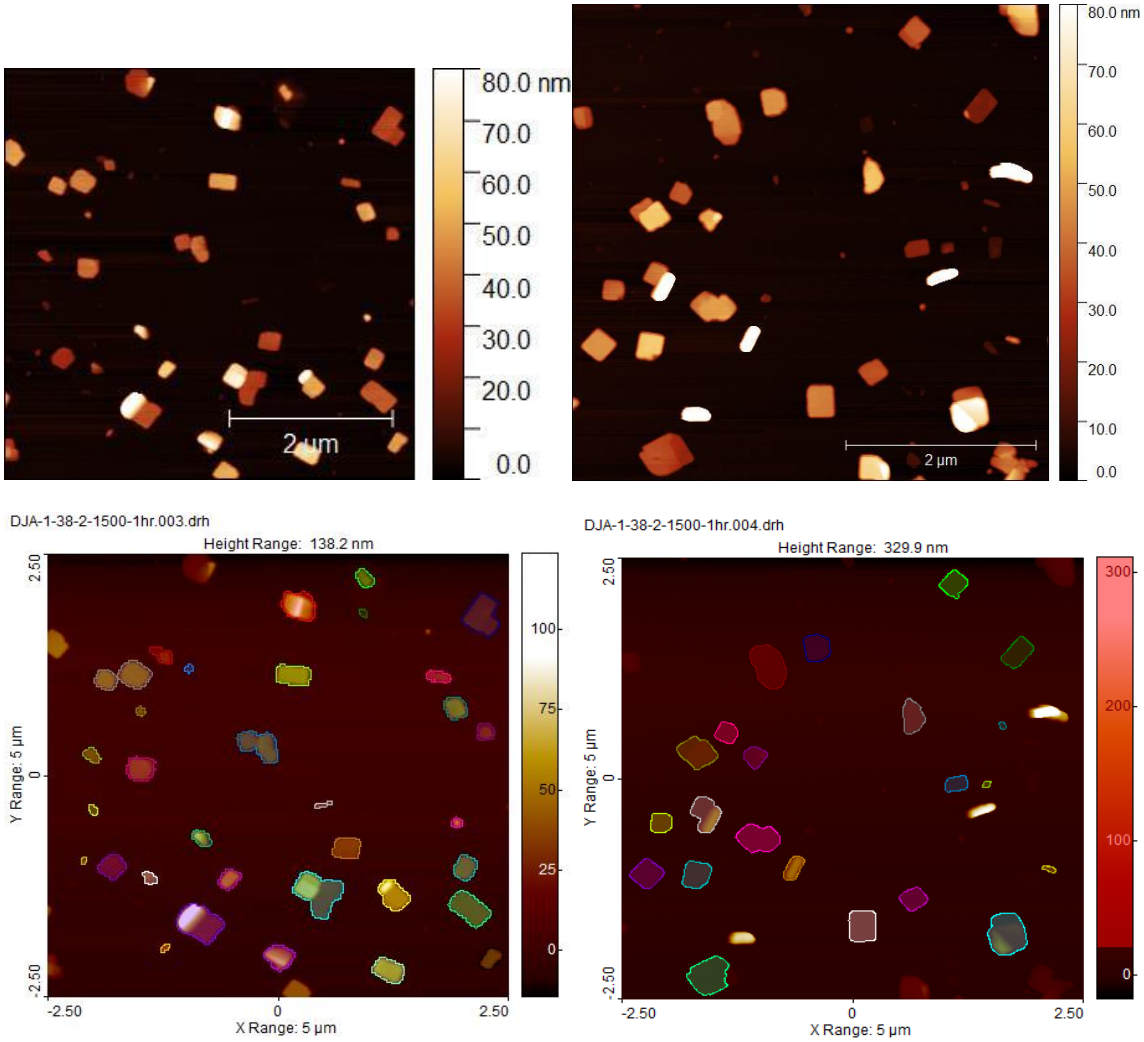

Figure S32. AFM topographical images of **2,5**-MTV-MOF exfoliated in MeCN and centrifuged at 1500 rpm for 1 hr, and automated particle identification.

2.5.Tertiary and higher blends of MTV-MONs

2.5.1. PXRD

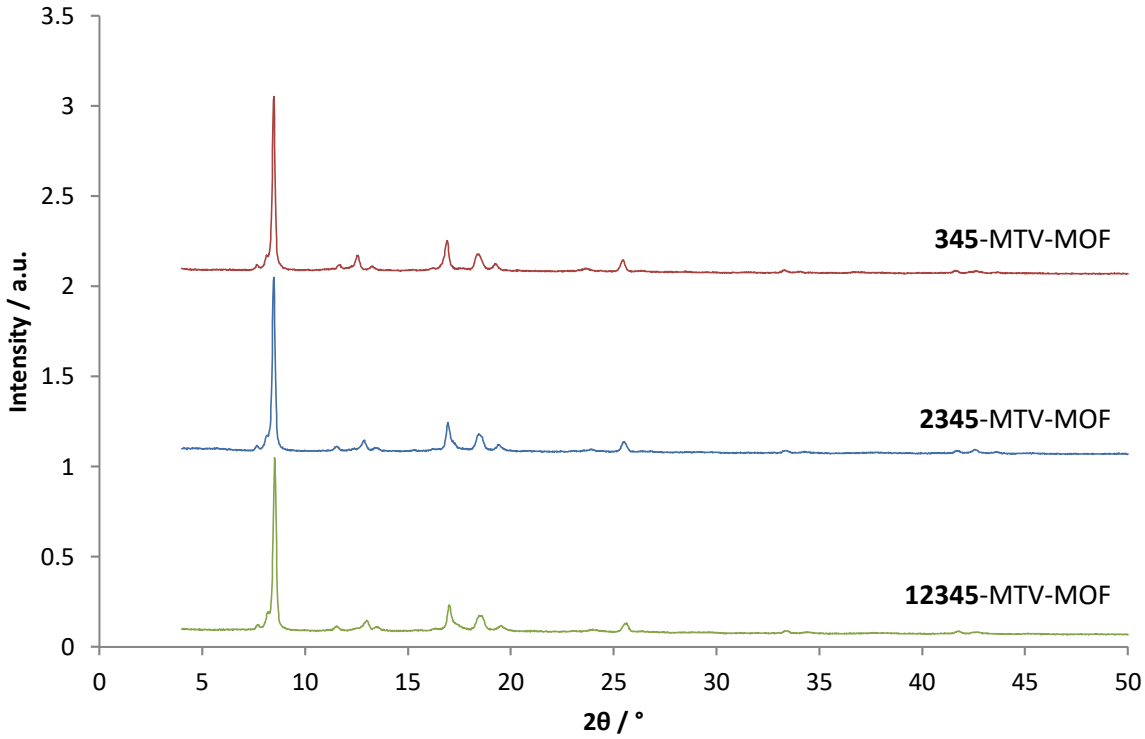

Figure S33. PXRD patterns of MTV-MOFs recollected after exfoliation in MeCN.

2.5.2. AFM

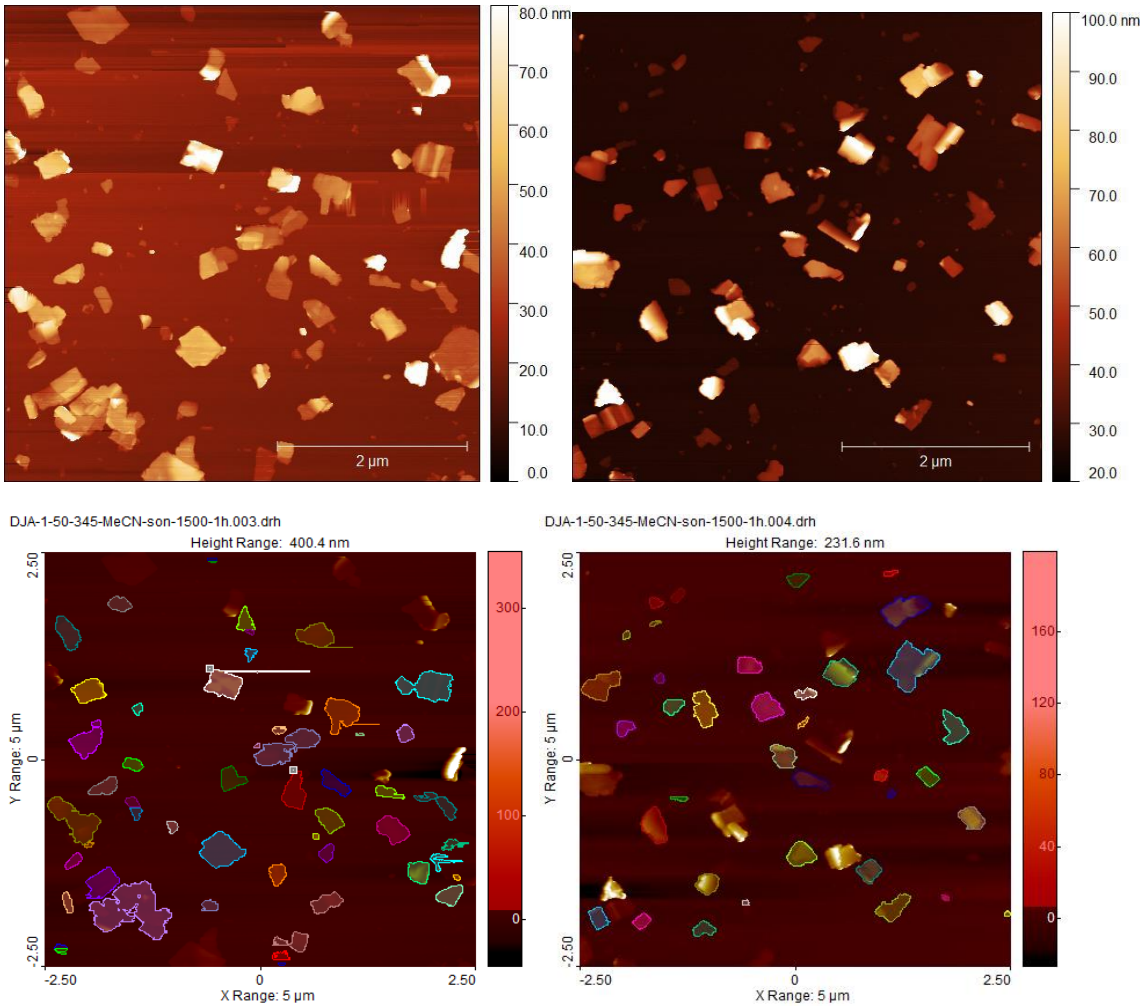

Figure S34. AFM topographical images of **345**-MTV-MOF exfoliated in MeCN and centrifuged at 1500 rpm for 1 hr, and automated particle identification.

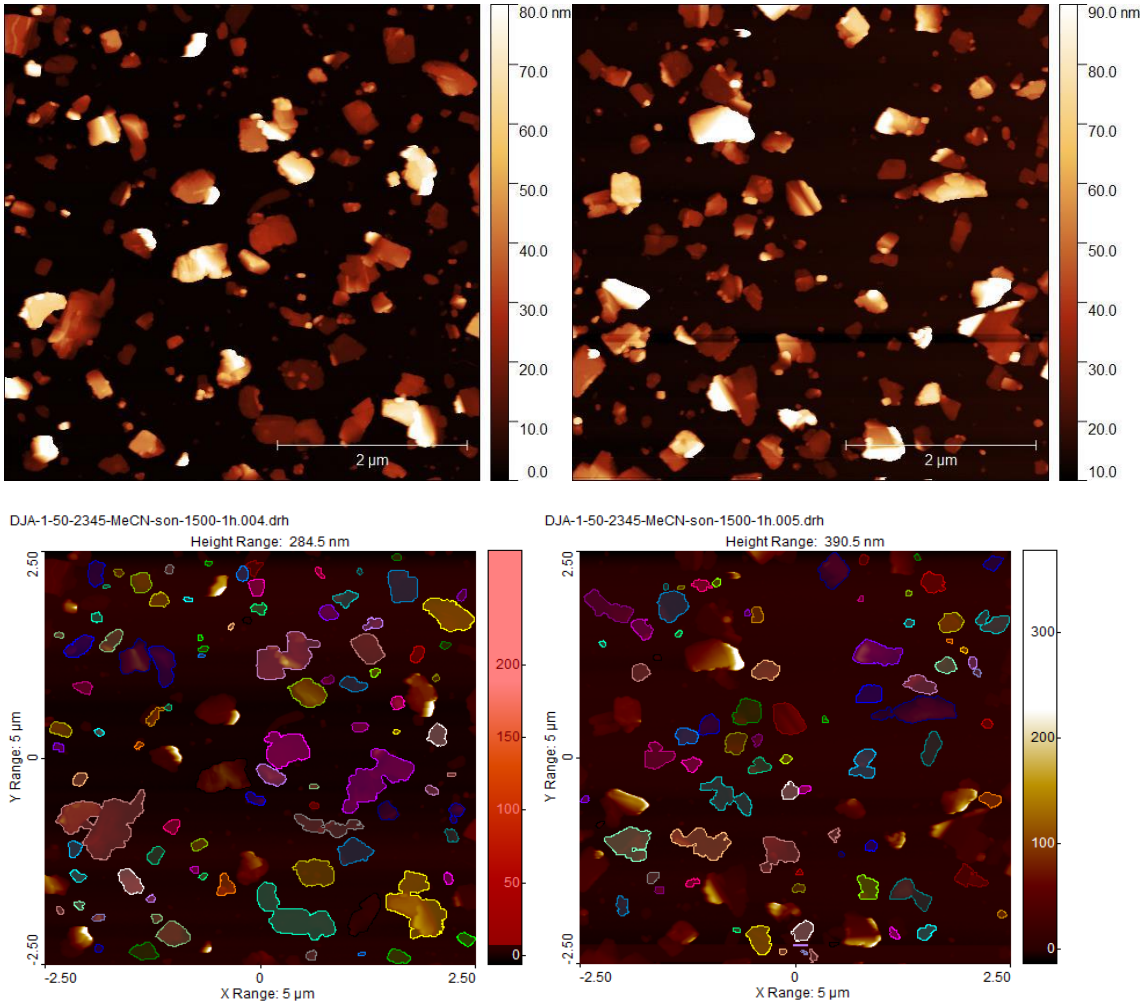

Figure S35. AFM topographical images of **2345**-MTV-MOF exfoliated in MeCN and centrifuged at 1500 rpm for 1 hr, and automated particle identification.

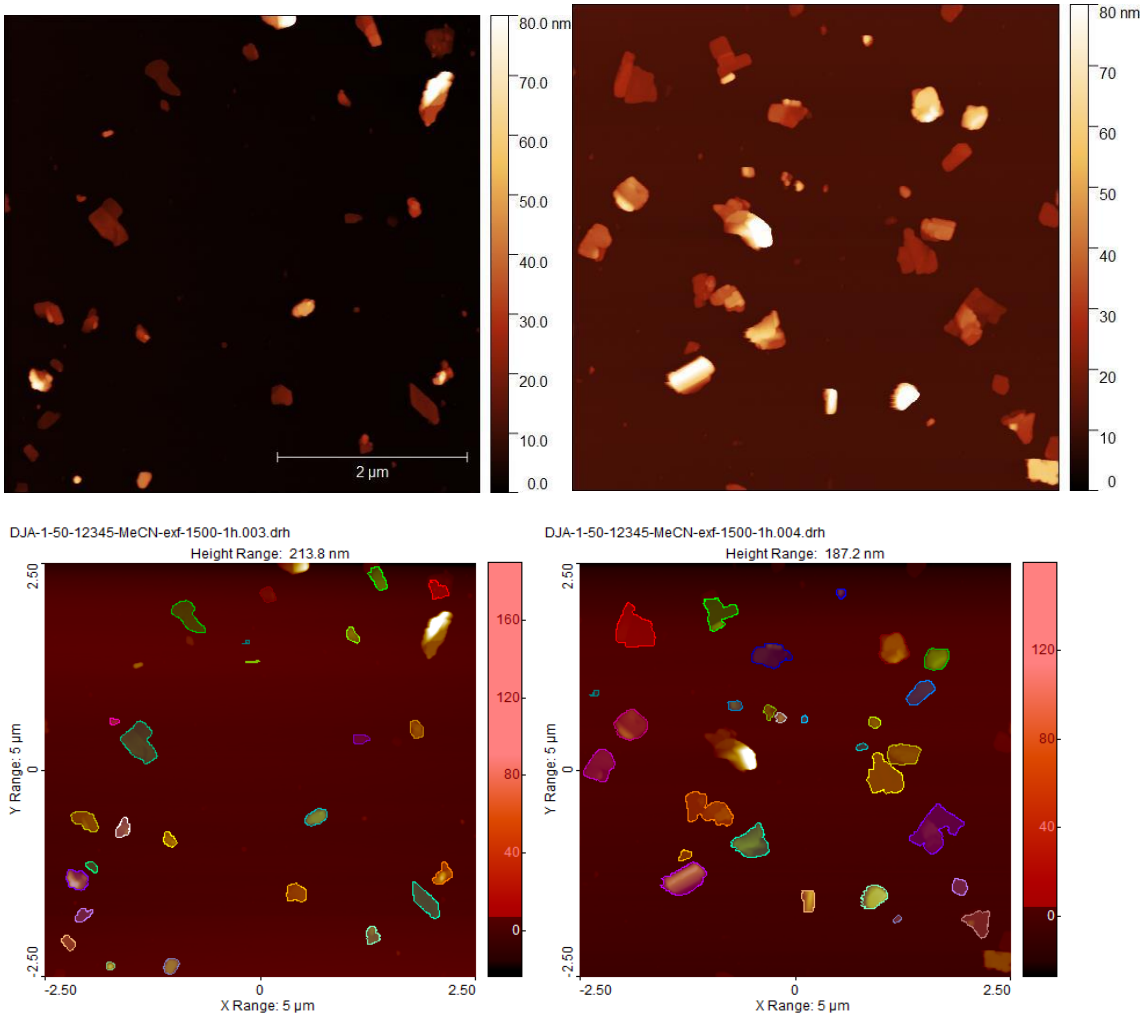

Figure S36. AFM topographical images of **12345**-MTV-MOF exfoliated in MeCN and centrifuged at 1500 rpm for 1 hr, and automated particle identification.

3. SPIP particle sizing

Automated particle sizing using SPIP software has both advantages and disadvantages over hand-sizing methods.[4] It is much faster, and eliminates subjective human error, particularly over height measurements where a MON may not be a single uniform height. The SPIP sizing output of "z mean" gives the average z (i.e. height) across an identified particle, which may be more informative than a single profile across a particle, as is often observed within the literature.

However, accurate sizing relies on high-quality AFM images with excellent particle/background resolution. The sample preparation is also therefore paramount, as the software cannot identify overlying particles, and instead treats these as single entities, which potentially corrupts results with erroneous measurements.

Within the manuscript, we presented size data for single ligand MOFs 3-5 and 5*. MONs were resized from raw data presented in previous studies.[1,3] A comparison of average particle size data is presented in Table S6. Generally, average lengths are larger (<20 %) when sizing with SPIP. This may result from slightly overlapping particles that can be individually sized by hand, but the software reads as single entities. Average heights are consistently lower when sized using SPIP. This is a result of the differing sizing methods: previous studies sizing the height by hand take the largest height of each particle, however SPIP parameter used was the average height of the whole particle (this is not readily available when sizing by hand). Trends for both length and height across the data series are consistent between hand sizing and SPIP, giving confidence to results.

Table S6. Average particle size data for single-ligand MONs, using SPIP automated particle sizing and hand-sizing methods

MOF	Length / nm		Height / nm	
	Hand	SPIP	Hand	SPIP
3	222±95	285±151	35±26	26±17
4	275±148	305±162	22±13	17±10
5	348±202	334±195	19±10	14±8
5*	512±234	587±262	59±234	35±18

Table S7. Summary of MON average particle size data determined by SPIP, and hydrodynamic diameter according to DLS.

MON	n	Length	Height	AR*	Diameter†
5,5*-MTV-MON	187	280±217	14±10	29±29	210
3,5-MTV-MON	62	333±223	18±10	20±12	221
2,5-MTV-MON	55	315±133	33±17	11±6	197
2,3-MTV-MON	70	196±87	12±6	18±8	109
345-MTV-MON	90	319±204	20±11	18±10	214
2345-MTV-MON	173	263±201	20±10	14±10	215
12345-MTV-MON	53	294±148	21±12	18±12	186

All size values are in nm. *AR=aspect ratio, defined as length/height (calculated for each particle). †Hydrodynamic diameter according to number average DLS data.

Particle size distributions

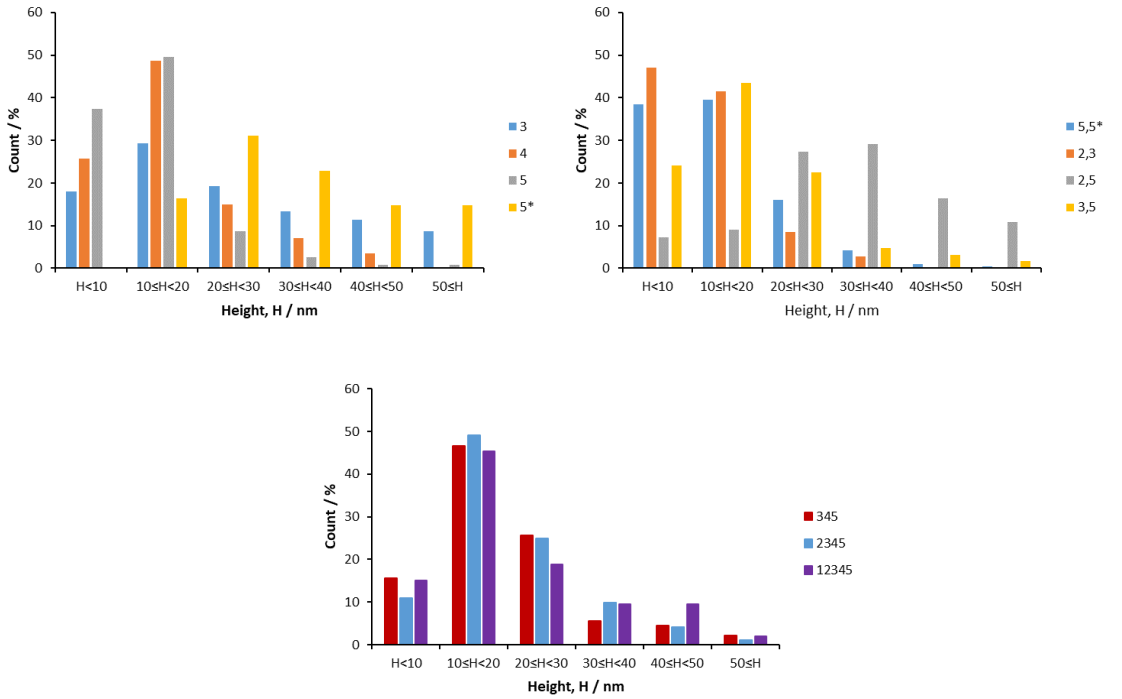

Figure S37. Height distributions for the different MONs analysed using SPIP software. Legends indicate the ligands incorporated into the MOFs as synthesised before exfoliation to MONs, for example 3 = **3**-MOF, and 345 = **345**-MTV-MON.

4. References

1 D. J. Ashworth, T. M. Roseveare, A. Schneemann, M. Flint, I. Dominguez Bernáldes, P. Vervoorts, R. A. Fischer, L. Brammer and J. A. Foster, *Inorg. Chem.*, 2019, **58**, 10837–10845.

2 J. A. Foster, S. Henke, A. Schneemann, R. A. Fischer and A. K. Cheetham, *Chem. Commun.*, 2016, **52**, 10474–10477.

3 D. J. Ashworth, A. Cooper, M. Trueman, R. W. M. Al-Saedi, S. D. Liam, A. J. Meijer and J. A. Foster, *Chem. - A Eur. J.*, 2018, **24**, 17986–17996.

4 C. Backes, D. Hanlon, B. M. Szydlowska, A. Harvey, R. J. Smith, T. M. Higgins and J. N. Coleman, *J. Vis. Exp.*, 2016, **2016**, 10–13.